

## *Original*

Mueller, S.; Stanev, E.V.; Schulz.Stellenfleth, J.; Staneva, J.; Koch, W.:  
**Atmospheric boundary layer rolls: Quantification of their effect  
on the hydrodynamics in the German Bight**  
In: Journal of Geophysical Research (2013) AGU

DOI: [10.1002/jgrc.20388](https://doi.org/10.1002/jgrc.20388)

## Atmospheric boundary layer rolls: Quantification of their effect on the hydrodynamics in the German Bight

Sabine Müller,<sup>1</sup> Emil V. Stanev,<sup>1</sup> Johannes Schulz-Stellenfleth,<sup>1</sup> Joanna Staneva,<sup>1</sup> and Wolfgang Koch<sup>1</sup>

Received 4 July 2013; revised 5 September 2013; accepted 8 September 2013; published 7 October 2013.

[1] Atmospheric boundary layer rolls and their impact on upper ocean circulation were investigated using a combination of two high-resolution data sources: (1) data from the Advanced Synthetic Aperture Radar (ASAR) onboard ENVISAT with a spatial sampling of approximately 500 m × 500 m and (2) continuous observations taken at the research platform FINO 1 with 2 min temporal sampling at eight heights between 33 and 100 m. The parallel analysis of instantaneous image data in combination with the FINO 1 time series enabled us to quantify both the spatial and temporal dynamics of mesoscale and submesoscale wind variations. The influence of these variations with different temporal and spatial scales on the hydrodynamics of the German Bight was addressed using outputs from a three-dimensional circulation model. It was demonstrated that while the coupling between wind and tidal forcing triggered substantial responses at mesoscales, the response of surface currents and sea surface temperature to the atmospheric boundary layer rolls appeared relatively weak. However, these ocean surface responses closely follow the surface footprint of the atmospheric boundary layer rolls, the signatures of which become more pronounced in the absence of strong tidal flows.

**Citation:** Müller, S., E. V. Stanev, J. Schulz-Stellenfleth, J. Staneva, and W. Koch (2013), Atmospheric boundary layer rolls: Quantification of their effect on the hydrodynamics in the German Bight, *J. Geophys. Res. Oceans*, 118, 5036–5053, doi:10.1002/jgrc.20388.

### 1. Introduction

[2] Synthetic aperture radars (SAR) are able to visualize the patterns of small-scale roughness on the surface of the ocean and, as a result, can reveal a plethora of footprints indicative of processes taking place both within the water body and in the overlying atmosphere. SAR images (Figure 1, left column) often show regular streak-like features caused by the boundary layer rolls (BLR) in the marine atmospheric boundary layer [Fu and Holt, 1982; Thompson *et al.*, 1983; Alpers and Brümmer, 1994; Young *et al.*, 2002]. BLR are coherent atmospheric structures that occur in persistent counterrotating vortical rolls along a horizontal axis that is approximately aligned with the mean wind direction. Their wavelengths vary between 2 and 20 km while downstream they can extend from 10 to 100 km [Etlting and Brown, 1993]. They occur due to thermal or dynamical instabilities of the boundary layer and often develop in concert with cold-air outbreaks [Müller *et al.*, 1999; Gryschka and Raasch, 2005; Gryschka *et al.*, 2008] or hurricanes [Wurman and Winslow, 1998; Katsaros *et al.*, 2000; Foster, 2005; Morrison *et al.*, 2005]. Presently,

we can only partially decipher the meaning of BLR as they appear in radar images and quantify their impact on processes in the atmosphere and ocean. We know that wind modulates the spectrum of short Bragg waves, which makes it possible to “see” BLR in SAR images. However, we are uncertain of the detailed nature of BLR imprints on the ocean surface and whether some of the consequences of this imprint (such as changes in temperature or surface current) are actually large enough to be detected by instrumental techniques that are presently available. The present paper addresses these two issues.

[3] Rolls similar to those observed by Alpers and Brümmer [1994] in SAR images of the German Bight between September 2005 and September 2009 motivated further analysis of their potential impact on the underlying ocean. For example, the study of Zhang *et al.* [2008] suggests that the roll vortices may be a significant factor in modulating the air-sea momentum exchange mixing the boundary layer more efficiently than local turbulent diffusion. In the coastal ocean, such structures are expected to impact mixing and matter transport.

[4] Because the scales of BLR are closely related to the dominating dynamics, we will specify here the terminology used. Structures and processes that develop on lateral scales of a kilometer will be termed as submesoscale. In more general terms the submesoscales are characterized by  $O(1)$  Rossby number dynamics, that is, the quasi-geostrophic approximation is not applicable. In the atmospheric classifications submesoscale processes are smaller than 2 km.

[5] Another mesoscale feature, the Langmuir circulation, is an oceanic phenomenon whose surface effects are in

<sup>1</sup>Institute of Coastal Research, Helmholtz-Zentrum Geesthacht, Geesthacht, Germany.

Corresponding author: E. V. Stanev, Institute of Coastal Research, Helmholtz-Zentrum Geesthacht, Max-Planck-Str. 1, 21502 Geesthacht, Germany. (emil.stanev@hzg.de)

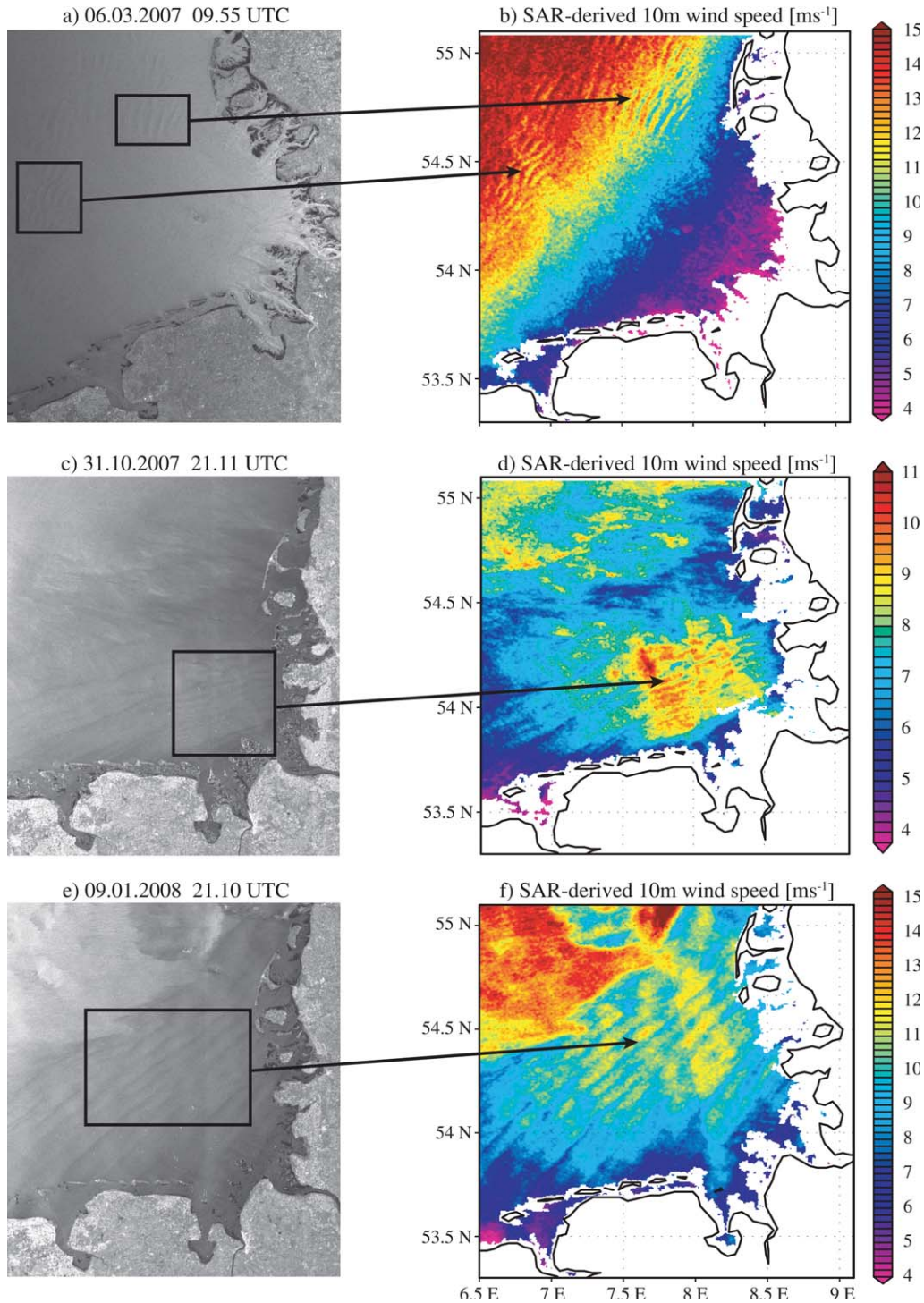


**Figure 1.** (a, c and e) Three SAR images showing streak patterns in the area of the German Bight and (b, d and f) their associated 10 m wind fields retrieved by the WiSAR method (see text). The estimated wave length of the variations is between 5 km (in Figures 1a and 1c) and 10 km (in Figure 1e). Different amplitudes of the wind variations were observed: 1–1.5  $\text{ms}^{-1}$  (Figure 1b), about 0.5  $\text{ms}^{-1}$  (Figure 1d), and 0.5–0.8  $\text{ms}^{-1}$  (Figure 1f).

some respects similar to those generated by BLR and hence it is important to clarify the similarities and differences between the two processes. Regularly spaced lines of foam, which are sometimes visible on the ocean surface were explained by *Langmuir* [1938] as due to local flow conver-

gence, with downward motions beneath the rows compensated by an upward flow in between. The separation of bands generally ranges from about 2 m to 1 km and their lengths are up to 10 times larger. Geometrically, the Langmuir circulation represented as vortices of alternating signs

with horizontal axes directed downwind, is similar to the helical structure of the BLR, although their dynamics depend on the Stokes drift induced by surface waves [Leibovich, 1983; Thorpe, 2004]. In contrast, the helical motions in the atmosphere are not driven by wind waves. Rather, the convective instabilities in the boundary flow determine the dynamics of atmospheric BLR.

[6] The strong interest in developing fine resolution wind products was partially satisfied by the QuikSCAT satellite radar scatterometer, which at a scale of about 25 km revealed the existence of persistent small-scale features in the wind stress [Chelton *et al.*, 2004]. However, there are important short-scale processes, which cannot be captured at the QuikSCAT resolution. Monaldo *et al.* [2004] demonstrated that QuikSCAT and RADARSAT-1 (SAR) measurements can be combined to provide better high-resolution wind data in coastal areas than either instrument can offer alone. Small-scale features in ocean winds were studied recently by Signell *et al.* [2010] using the Bora wind events. The Bora is known to contain multiple jets, yet the detailed spatial structure of these jets (about 10 km) cannot be resolved by the available traditional in situ observations. SAR data appear to contribute to solving this coastal ocean problem.

[7] The present paper compares mesoscale features observed in satellite data with in situ observations obtained from research platforms in order to establish the consistency and complementarity of the different data sources. This is a prerequisite for the intercalibration of observations, improving quality of existing estimates and developing new ocean wind products, in particular, with regard to the smaller scales. Therefore, one of the motivations of the present study is to demonstrate the synergy between these different data sets.

[8] Some issues related to SAR-derived wind data, such as (1) limited temporal sampling and (2) coarse resolution of wind direction, underline the need for synergy with other data sources. By statistically combining SAR data and data from numerical weather predictions (NWP), Portabella *et al.* [2002] contributed to establishing the consistency between these different data sources. Horstmann and Koch [2005], Koch and Feser [2006], and Beaucauge *et al.* [2007] compared wind assessment in coastal waters from SAR and NWP models and demonstrated that SAR satellite imagery and NWP models provided reliable estimates of fine-scale surface wind fields.

[9] In addition to surface wind variations, it is also known that oceanic phenomena can modulate the radar cross section as imaged by a SAR system. This is typically seen in shallow areas when small-scale features of the bathymetry cause strong current gradients, which then in turn modulate the spectrum of the short Bragg waves [Alpers and Hennings, 1984]. Similar effects can also be observed in the presence of strong internal waves [Kropfli *et al.*, 1999] or upwelling [Kozlov *et al.*, 2012]. In some cases, specific patterns can be detected on a SAR image even if the wind field in the area is homogeneous. However, the situation we consider here for BLR is different in the sense that we take the modulations in the SAR image to be primarily caused by variations in the near-surface wind field, as suggested by Stoffelen and Anderson [1997], who demonstrated that the BLR signature can be explained in this

way. This provides a basis to develop a standard procedure for determining winds over the oceans by SAR satellite observations. However, we also want to know whether the atmospheric BLR cause a measurable imprint in the upper ocean.

[10] Because the ocean responses to small-scale wind forcing in the coastal zone with different temporal and spatial scales are not well known, and because this is partially due to the lack of continuous observations over larger areas, it is helpful to perform dedicated numerical experiments. The motivation to do this stems from the fact that numerical simulation of the impact of BLR on ocean currents has not received much attention so far. Based on the analysis of observations, a “synthetic” wind forcing was constructed in the present study, which was used to drive several sensitivity experiments. Results presented herein demonstrate that the parallel use of available data sets could help to improve the forcing data for the coastal ocean. The data used in this study are described in section 2. In section 3, small-scale wind patterns observed on 6 March 2007 were analyzed conjointly with wind data measured at the FINO 1 platform. In section 4, results from sensitivity studies of the ocean model responses are presented. The results are summarized in section 5.

## 2. Data

### 2.1. Wind Data From SAR

[11] The primary mechanism of microwave backscattering from the sea surface is Bragg scattering. Many satellite-borne SAR systems operate at C-band with moderate incidence angles between 15° and 50°. For the electromagnetic wavelength of about 5 cm and the incidence angles of 15–50°, the backscatter of the ocean surface is primarily caused by the small-scale ocean surface roughness with a horizontal scale of a few centimeters. As this is primarily influenced by the local wind stress, it is possible to relate the radar backscatter to the near-surface wind field.

[12] SAR data used in the present paper originate from the advanced synthetic aperture radar (ASAR) on board ENVISAT. High-resolution wind fields at 10 m height were retrieved by the wind retrieval from SAR (WiSAR) method, which is described in Koch [2004] and presents a two-step process. In the first step, wind directions were extracted from wind-induced streaks, which were aligned with wind direction and which were visible on SAR images. Orientations of these streaks were extracted by using the local gradient (LG) method [Horstmann *et al.*, 2002; Koch, 2004]. In the second step wind speeds were retrieved from the backscattered normalized radar cross section (NRCS) of the ocean surface by utilizing a geophysical model function (GMF), which describes the dependence of the NRCS on the wind and radar imaging geometry [Horstmann and Koch, 2005].

[13] At wind speeds below 25 ms<sup>-1</sup>, WiSAR is capable of retrieving winds with a typical error of about 20° in wind direction and 2 ms<sup>-1</sup> in wind speed [Horstmann *et al.*, 2003; Horstmann and Koch, 2005; Koch and Feser, 2006].

[14] Well-pronounced mesoscale and submesoscale patterns over the German Bight are identified from SAR images (Figures 1a, 1c, and 1e). The SAR-derived 10 m

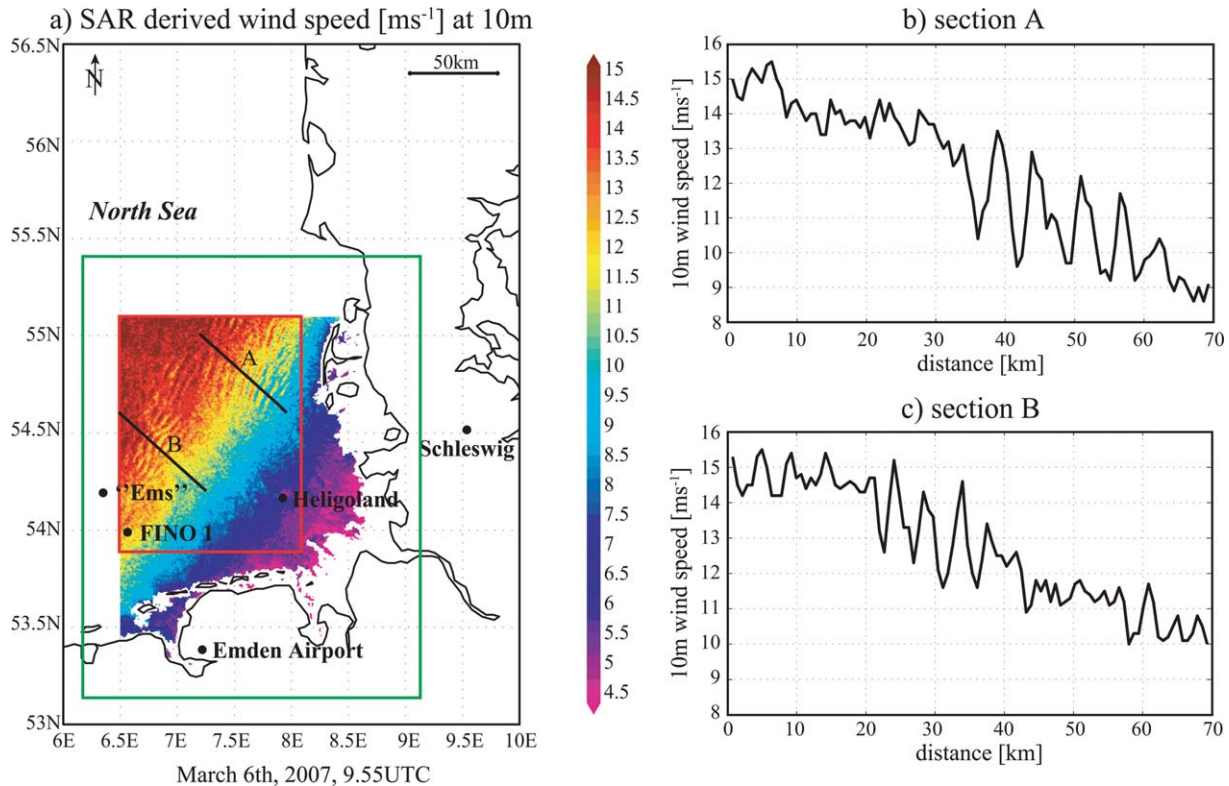


**Figure 2.** (a) SAR-derived wind speed within the area of the German Bight on 6 March 2007, 9.55 UTC. Streak patterns can be seen along the section A and B (black lines). The observed angle between the streak alignment and the zonal direction is between  $55^\circ$  and  $65^\circ$ . The black points denote the locations of research platform FINO 1, MARNET station “Ems” and the places of radio soundings in Schleswig and at Emden Airport. The area within the red rectangle was analyzed by means of FFT (see section 3.1). It is about 105 km in zonal and 134 km in meridional direction. The green-bounded area is the model area where numerical experiments are performed. (b) See the 10 m wind speed along (b) section A and along (c) section B. The profiles are oriented from northwest to southeast. Periodic variations can be seen between kilometer 35 and 65 (section A) as well as between kilometer 20 and 40 (section B).

wind fields (Figures 1b, 1d, and 1f) show even more clearly a number of periodic wind streaks. In the following, deeper consideration will be given to the image of 6 March 2007 (Figures 1a and 1b) with the aim of demonstrating the BLR-character of mesoscale patterns. The corresponding SAR data were acquired at vertical polarization during an ascending pass at 9.55 UTC and with a pixel size of about 500 m.

## 2.2. Wind Data From the FINO 1 Platform

[15] FINO 1 is a research platform in the German Bight located at  $54.02^\circ\text{N}$ ,  $6.58^\circ\text{E}$  about 45 km north of the Borkum Island (see Figure 2a). Cup anemometers measure wind speed at 33, 40, 50, 60, 70, 80, 90, and 100 m (Figure 3, top), whereas the deck of the platform with the wind tower is at 20 m above CD (chart datum). Raw data of observed wind speed and wind direction, which is measured with vanes at 33 and 90 m height, are used to analyze small-scale wind structures. The data with a temporal sampling of 2 min were provided by the Federal Maritime and Hydrographic Agency (BSH). Data gaps were filled using spline interpolation.

[16] The wind speed data at the different heights correlate well with a coefficient of 0.99 between 33 m and each

given height, i.e., there is almost no wind shear detectable between 33 and 100 m height and the instrument noise appears to be small.

[17] The cup anemometers of FINO 1 platform are installed on booms on the southeast side of the mast, while the wind vanes are on the northwest side. Wind speed reduction effects due to the mast can be observed at the cup anemometers if wind is northwesterly, i.e., for wind directions between  $300^\circ$  and  $340^\circ$ . (Here and in the following, the meteorological convention for wind direction and the oceanographic one for current’s direction are used.) The smallest disturbance is expected if wind is coming from  $45^\circ$  to  $225^\circ$  (Westerhellweg et al., presentation at EWEA-2011 Conference, Brussels, Belgium). Because a southerly wind was dominant, significant mast shadowing effects for the cup as well as for the vane measurements are not expected.

## 2.3. Additional Data Sources

[18] To support the following analysis further, data sources describing the atmospheric state in the German Bight were used. Radiosonde data were provided by the University of Wyoming. The observations were taken in Schleswig and at Emden Airport (Figure 2a) on 6 March 2007 at

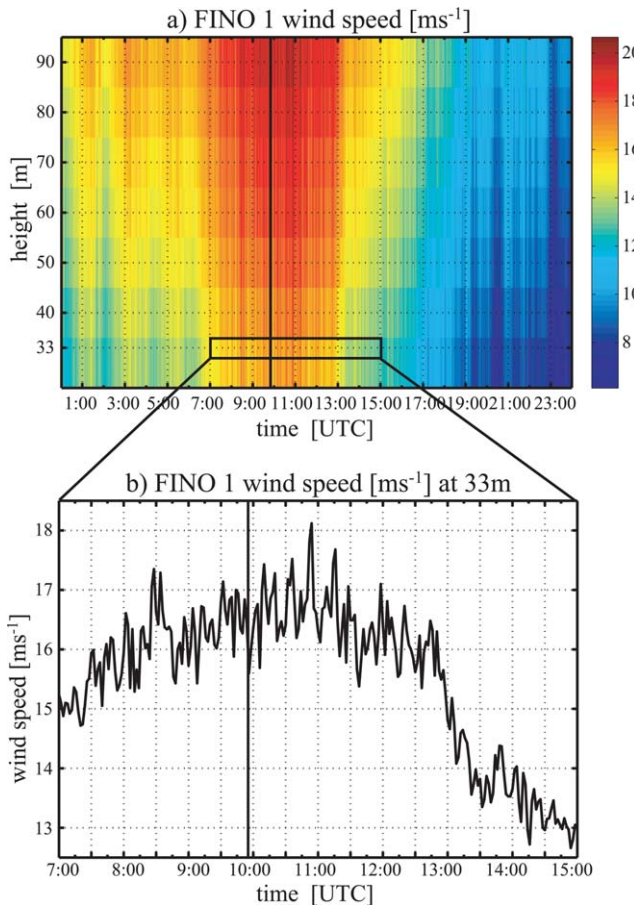


**Figure 3.** (a) Wind speed at different heights measured at FINO 1 platform on 6 March 2007. The black line denotes the time of SAR observation. (b) Wind speed at 33 m height between 7 and 15 UTC.

12 UTC. Wind speed, wind direction, air temperature, and potential temperature of the radio soundings were used to get an idea of the vertical structure of the atmosphere.

[19] The weather chart used here is the Berliner Wetterkarte for 0 UTC and 12 UTC (Figure 4) provided by the Freie

Universität Berlin. This analysis surface weather map gives information about sea level pressure and fronts. Upper level charts as well as maps of hourly station observations provided by the Freie Universität Berlin (not presented here) also provide information about precipitation and cloud cover around the SAR observation time. Furthermore, the FINO 1 data base also includes observations of precipitation and cloud cover.

[20] The 10 m wind field, sea level pressure, total cloud cover as well as temperature and dew point at 2 m height on a 0.2° grid can be obtained from six hourly surface reanalysis data provided by the European Centre for Medium-Range Weather Forecasts (ECMWF), which were also used in the numerical part of this paper (see section 4).

[21] Water temperature observations were available from the Marine Environmental Monitoring Network in the North Sea and Baltic Sea (MARNET) station “Ems,” which is an unmanned lightship located at 54.2°N, 6.35°E (Figure 2a). The data are available hourly or as daily averages provided by the BSH.

[22] All these data were used to investigate the meteorological conditions under which the analyzed SAR image was acquired.

### 3. A Case Study of SAR-Observed Boundary Layer Rolls

#### 3.1. Wind Data From the SAR Image of 6 March 2007

[23] The SAR-derived wind field from 6 March 2007 (Figure 2a) exhibited several streak-like structures to the west of the Danish Peninsula. The 10 m wind field in the German Bight at the time of image acquisition can be characterized by an almost linear increase with distance to the coast. Wind speeds of about 5 ms<sup>-1</sup> were observed in the coastal zone and increased to about 15 ms<sup>-1</sup> in the north-western part of the studied area. Coherent patterns can be seen in regions where the wind speed was larger than about 10 ms<sup>-1</sup>. The amplitude of the periodic wind variations, which were observed along sections A and B, is in the range of 1–1.5 ms<sup>-1</sup> (Figures 2b and 2c).

[24] The region of the German Bight (red rectangle in Figure 2a) is analyzed below with respect to the

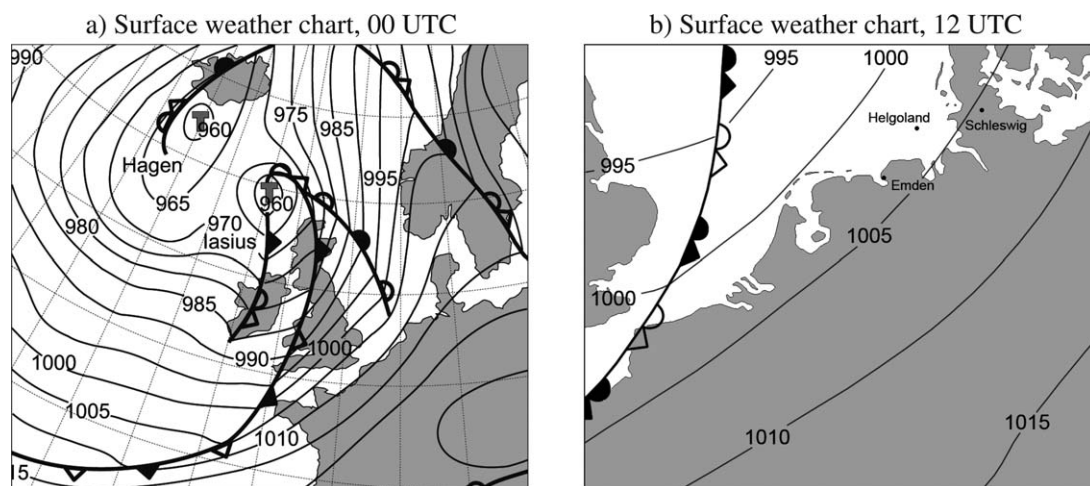


**Figure 4.** (a) Surface weather chart replotted from the “Berliner Wetterkarte” from 6 March 2007, 0 UTC. (b) The weather chart from 12 UTC is only available for the southern North Sea and the coastal area.

corresponding wind variations. The considered area is about 105 km in zonal and 134 km in meridional direction and contains  $211 \times 269$  SAR data points. A two-dimensional spectrum  $P_i$  was computed using a fast Fourier transformation (FFT). The spectrum was scaled with respect to the maximum value, the logarithm was taken, and a Gaussian filter was applied (Figure 5). Most energy is contained at scales of 5–6 km, which exceeds the upper bound of the submesoscale range. The mean wavelength of the streaks is given by

$$\bar{\lambda}_{streak} = \frac{2\pi}{\bar{k}_{streak}}. \quad (1)$$

[25] Here, the scalar mean wave number  $\bar{k}_{streak}$  can be calculated as a weighted mean using the scaled spectral values  $P_i$ :

$$\bar{k}_{streak} = \frac{\sum_{i \in \mathbf{I}} (|\mathbf{K}_i| \cdot P_i)}{\sum_{i \in \mathbf{I}} P_i}, \quad (2)$$

where the magnitude of the wave vector  $\mathbf{K}_i$  with its components in zonal ( $k_i$ ) and meridional ( $l_i$ ) direction is  $|\mathbf{K}_i| = \sqrt{k_i^2 + l_i^2}$ , and  $\mathbf{I}$  is the set of indices  $i$  for which  $P_i \geq -1$ . The mean wavelength  $\bar{\lambda}_{streak}$  of the variations containing most energy computed in this way is 5.7 km.

[26] For a better understanding of the wind patterns, it is necessary to investigate the meteorological conditions, under which these streaks were formed. It can be assumed that the streaks were the footprints of atmospheric BLR as already described by *Alpers and Brümmer* [1994].

### 3.2. Meteorological Conditions on 6 March 2007

[27] On 6 March 2007, a low-pressure system called “HAGEN” was located to the south of Iceland as highlighted on the map of sea level pressure at 0 UTC in Figure 4a. Its secondary low IASIUS moved from about 60°N near the British Isles to the southern coast of Iceland. IASIUS generated a strong pressure gradient over the North Sea. High wind speeds of 15–20  $\text{ms}^{-1}$  were observed at the German coast and at various measurement platforms in the sea. Total cloud cover and intense rain were actually observed at the FINO 1 platform all day long as well as at the surface stations in the coastal areas from 5 UTC. Although Figure 4 does not enough resolve the temporal and spatial evolution of atmospheric fronts, it seems plausible that the synoptic situation had a warmfront character. This is supported by the analysis of the 850 hPa geopotential analysis maps (not shown) and the analysis of wind veering discussed further in this study. This gives important information on the formation mechanism of BLR considered here.

[28] Considering the synoptic regime on 6 March 2007, we will analyze below the potential of the atmosphere to develop BLR. The focus was set on the following two important instability mechanisms for their development [*Etling and Brown*, 1993]:

[29] A. An unstable temperature stratification in the atmospheric boundary layer (which develops when cold air flows over warm surfaces) can lead to the formation of BLR.

[30] B. A shear flow in the atmospheric boundary layer is favorable to the formation of BLR in spite of a neutral or

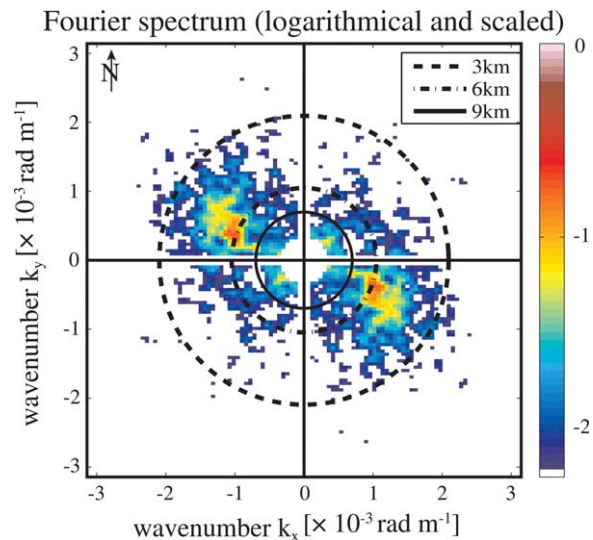


**Figure 5.** Two-dimensional spectrum of the SAR-derived 10 m wind field (see Figure 2a). Circles show the corresponding wavelength in kilometers. The wavelength of the dominant image features is between 5 and 6 km (red-colored maximum in the spectra) with an average of 5.7 km.

stable stratified atmosphere, if the vertical profile of the crosswind component  $v_{roll}(z)$  (aligned perpendicularly to the roll axis) exhibits an inflection point at the height  $z_i$ , which corresponds to a maximum in the vertical vorticity profile at the same height [*Etling and Brown*, 1993].

[31] With respect to the plausibility of mechanism (A), the vertical profiles of temperature and potential temperature from radio soundings at the stations Emden and Schleswig (Figure 2a) demonstrate that the air mass was stably stratified (Figure 6a), i.e., the gradient of potential temperature was about 0.2–0.7 K per 100 m, which supports the plausibility of warm air advection. Thus, no convective conditions were present on 6 March 2007. In addition, the water temperature  $T_w$  observed at the MAR-NET station “Ems” (about 7°C) was lower than the near-surface air temperature measured by the radiosonde in Emden (8.6°C at 5 m height). Therefore, process (A) was not the driver for generating BLR on 6 March 2007.

[32] With respect to mechanism (B), the vertical wind profiles at the stations Emden and Schleswig were transformed into the components  $u_{roll}$  and  $v_{roll}$  in the rotated coordinate system  $\Sigma_{roll}$  (Figure 7) using the equations

$$u_{roll} = u \cos \beta + v \sin \beta \quad (3)$$

$$v_{roll} = -u \sin \beta + v \cos \beta, \quad (4)$$

where  $\beta = 55^\circ$  is the angle between the roll orientation and the east direction estimated from the SAR wind data. The profiles of  $u_{roll}$ , defined as the wind component parallel to the axis of the BLR, and  $v_{roll}$ , defined as the cross component, (Figures 6b and 6c), demonstrated that there was a strong wind of nearly 23 and 28  $\text{ms}^{-1}$  at 1000 m height. The cross-component  $v_{roll}$  at the Schleswig station exhibited an inflection point at about 1000 m height. At the same time the wind profile in Emden was approximately linear between 300 and 1600 m height.

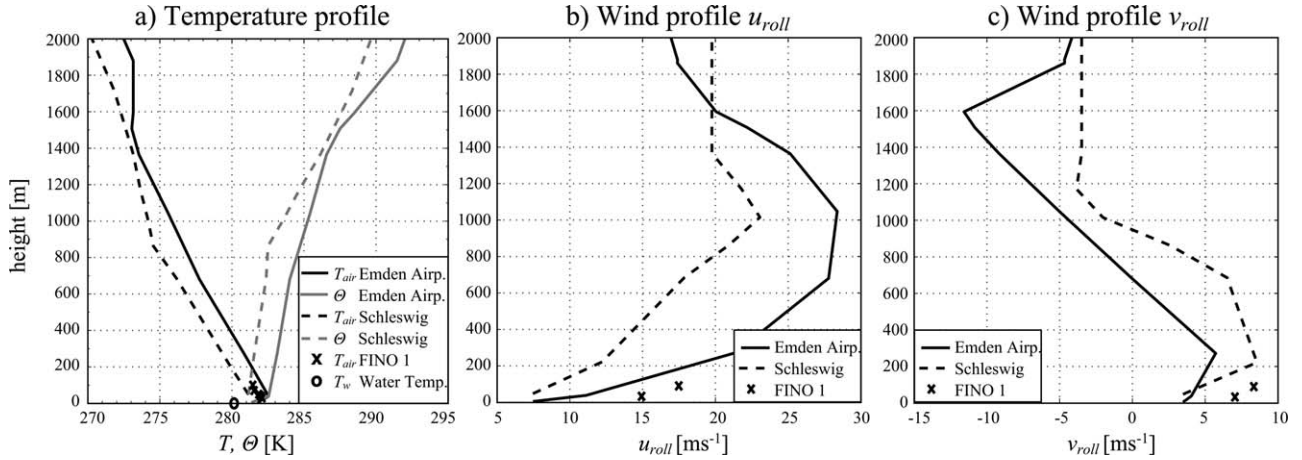


**Figure 6.** Vertical profiles of (a) temperature  $T_{air}$  and potential temperature  $\Theta$ , (b)  $u_{roll}$ , the wind component parallel to the roll axis, and (c)  $v_{roll}$ , the cross component. The data were observed at Emden Airport (solid lines), Schleswig (dashed lines) and FINO 1 platform (x) on 6 March 2007 at 12 UTC. In Figure 6a,  $T_w$  is the water temperature observed at the MARNET station “Ems.”

[33] From the above considerations, it seems that the inflection point instability (mechanism B) is the plausible cause of generating the BLR on 6 March 2007. The above case is very similar to the event on 2 January 1992 over the Jade-Weser estuary that was investigated by *Alpers and Brümmner* [1994]. However, the wave length of the streak-like variations presented in *Alpers and Brümmner* [1994] varied between 1.2 and 2 km, which was three times smaller than the wave length reported above (almost 6 km). The resolution of 500 m used here is sufficient to, at least coarsely, resolve 6 km long waves. However, SAR data

gathered at a higher spatial resolution would be required to fully investigate the mesoscale dynamics in cases similar to that discussed by *Alpers and Brümmner* [1994].

### 3.3. FINO 1 Data

[34] Before 7 UTC, winds of 12–14  $ms^{-1}$  at 33 m height were observed characterized by a periodicity of 2 h (Figure 3a). This situation was followed by a period of high wind speed (15–18  $ms^{-1}$  at 33 m height), on which very short-time oscillations were superimposed. The aforementioned low-pressure system IASIUS was responsible for the

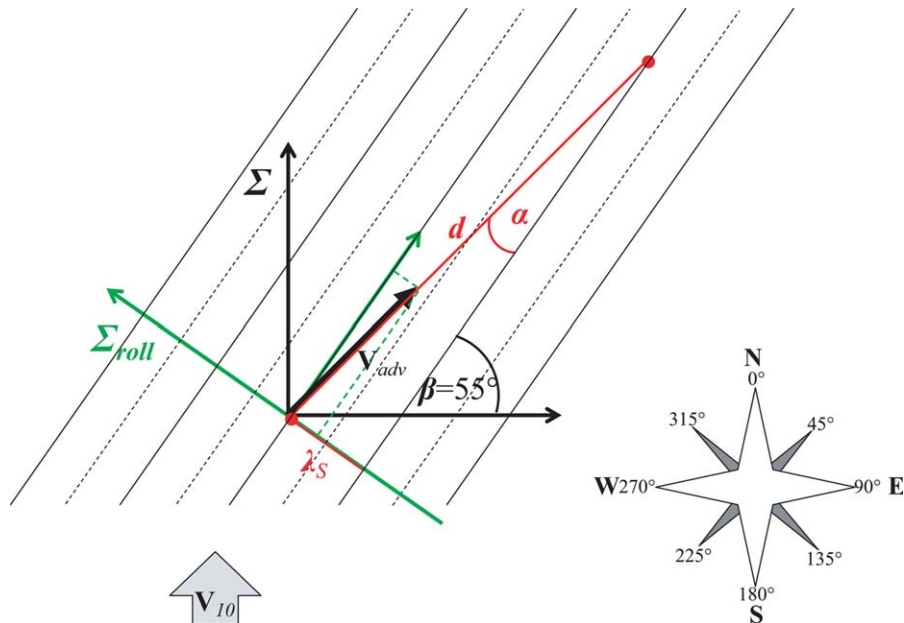


**Figure 7.** Illustration of the advection within the region of the wavestructure (black solid and dotted lines). The rolls are advected by  $V_{adv}$  from southwest (about 225°), which is e.g., a low-level jet at about 1000 m height. The distance  $d$  between two waves in direction of the advection can be calculated as  $d = \lambda / \sin \alpha$  with  $5 \text{ km} \leq \lambda \leq 6 \text{ km}$  and  $\alpha \approx 10^\circ$ , which is the angle between the roll inclination ( $\beta = 55^\circ$ ) and  $V_{adv}$ . The rotated coordinate system  $\Sigma_{roll}$  is orientated to the roll alignment. Vector  $V_{10}$  displays the wind direction at 10 m height.

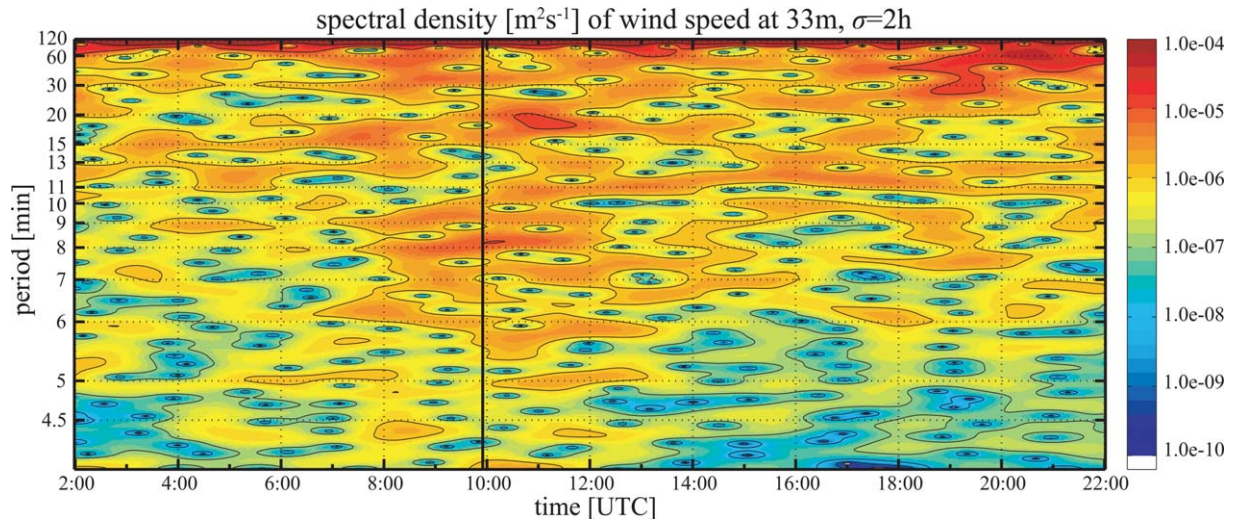


**Figure 8.** Distribution of spectral energy of the wind speed as a function of time and period, calculated from FINO 1 wind observations at 33 m height on 6 March 2007. The black line denotes the time of SAR observation.

stormy weather conditions. After 13 UTC, the wind slowly decreased and remained below  $8 \text{ ms}^{-1}$  at 33 m during the night.

[35] The wind directions observed at 33 and 90 m height (not shown here) were very similar. Wind blew from the south turning from  $167^\circ$  at 7 UTC to  $182^\circ$  at 10.30 UTC and  $190^\circ$  at 15 UTC. There was a slight counterclockwise wind rotation from 33 m to 90 m height during 8 and 13 UTC, but this wind veering in the Prandtl layer was negligibly small. As known from the radiosonde data of 12 UTC, the wind rotated clockwise with height from a southerly at about 200 m to a southwesterly at 1000 m, which is in the direction of veering observed within the Ekman layer. However, the difference between the turning angles of Ekman and observed veering gives an indication that an additional veering due to baroclinity (warm air advection) was superimposed.

### 3.4. Boundary Layer Roll Dynamics

[36] The following assumptions are made to identify the boundary layer rolls in the time series data. One can suppose that the advection speed of the BLR is to a large extent determined by the wind speed at the height of the inflection point (1000 m in the present case). The radiosonde data from 12 UTC exhibited a southwesterly ( $225^\circ$ ) low-level jet at approximately this height at speeds of about  $23 \text{ ms}^{-1}$  in Schleswig and  $28.8 \text{ ms}^{-1}$  in Emden. The evidence that the mean wind at FINO 1 platform did not change much during the previous 2 h facilitated the following analysis, justifying the use of the Taylor's hypothesis of frozen turbulence [Taylor, 1938]. This hypothesis assumes that the temporal variation at one point in space can be calculated as shown schematically in Figure 7. If the rolls drifted with a speed of  $\mathbf{V}_{adv}$ , the roll pattern as observed at some fixed location should repeat at a distance  $d$ , which can be calculated as

$$d = \frac{\lambda}{\sin \alpha}, \quad (5)$$

where  $\lambda$  was the wavelength in the range of 5–6 km and  $\alpha \approx 10^\circ$  the angle between the streaks alignment and the vector  $\mathbf{V}_{adv}$ . The corresponding period of the wind variations is

$$T = \frac{d}{|\mathbf{V}_{adv}|}. \quad (6)$$

[37] Periods of 17–25 min can be expected for wind speeds of  $23\text{--}28.8 \text{ ms}^{-1}$ .

[38] In order to present the theoretical estimates in a more objective way, a Fourier analysis was applied to the FINO 1 platform wind data at 33 m. A time versus period diagram (Figure 8) of the spectral energy at 33 m was computed using a sliding discrete Fourier transform [Jacobsen and Lyons, 2003], with a Gaussian window of 2 h width.

[39] There was an energy maximum with periods of 15 min (Figure 8) but an “energy gap” between 20 and 30 min in the early hours until 8 UTC. This situation changed during 8 and 14 UTC (the time when the storm passed over the German Bight), when the spectral power increased over a wider frequency range. A maximum at about 8 min can be found between 8 and 12 UTC, which can also be seen in the time series data in Figure 3a. During this period oscillations with periods of 7–10 min were stronger than at any other time of the day. Between 9 and 13 UTC, most energy was contained in periods of 17–26 min with a clear maximum at 11 UTC. This agrees well with our theoretical estimation that the observed BLR were advected by the low-level jet of  $23\text{--}28 \text{ ms}^{-1}$  and could be detected at the FINO 1 platform. After 14 UTC the stormy conditions subsided and energy decreased. A maximum can be seen for variations with 12 min period between 15 and 19 UTC. Variabilities of 30–60 min became dominant during the evening hours (about 19 UTC and later).

## 4. Coastal-Ocean Response to Wind Forcing With Different Scales

### 4.1. The Numerical Model

[40] There is a general consensus that updrafts and downdrafts associated with BLR can affect air-sea

momentum exchange [Zhang *et al.*, 2008]. Furthermore, by modifying sea surface roughness, mesoscale features additionally control processes in the atmospheric boundary layer and oceanic upper mixed layer. *Ginis et al.* [2004] proved that rolls play an important role in the boundary layer physics at high wind speeds.

[41] While the atmospheric boundary layer aspects of this problem seem well understood, it is not quite clear how important these oscillations are for the oceanographic processes. One way to address this issue is to analyze results of sensitivity numerical experiments, in which high-resolution wind fields can be generated artificially to represent small-scale features of the SAR-derived wind imagery.

[42] The model used here is the general estuarine transport model (GETM), which is a 3-D primitive equation numerical model [Burchard and Bolding, 2002], in which the equations for the three velocity components  $u$ ,  $v$ , and  $w$  and sea surface height  $\zeta$ , temperature  $T$ , salinity  $S$ , as well as the equations for the turbulent kinetic energy and the eddy dissipation rate due to viscosity are solved. Although part of the mechanical energy is passed to the ocean through the wind waves and Langmuir circulation could provide an additional mixing mechanism for momentum and tracers in the ocean mixed layer, the vertical mixing will be described in the numerical model just by a standard  $k$ - $\epsilon$  turbulence parameterization.

[43] The model set up for the area of our study (Figure 2a) is described by *Staneva et al.* [2009]. The horizontal discretization is done on a spherical grid. The model uses terrain-following equidistant vertical coordinates ( $\sigma$  coordinates). The vertical column is discretized into 20 nonintersecting layers. The numerical simulations are performed with nested-grid models consisting of a coarse resolution (about 5 km) North Sea-Baltic Sea outer model, and a fine-resolution (about 1 km) inner model covering the German Bight (green-bounded area in Figure 2). In the following, results from the fine-resolution model will be presented.

[44] The sea surface elevation at the open boundary of the North Sea-Baltic Sea model is generated using tidal constituents obtained from altimeter data via the OSU Tidal Inversion Software [Egbert and Erofeeva, 2002]. The model is forced by atmospheric fluxes that are computed from bulk aerodynamic formulas using model simulated sea surface temperature and 6 h atmospheric analysis data (2 m temperature and relative humidity as well as 10 m wind). In some of the numerical simulations, high-frequency atmospheric oscillations generated synthetically with 5 min discretization were used. Hourly river run-off data are provided by the BSH. Initial conditions for the period of our analysis starting on 6 March 2007 0 UTC used long-term simulations forced with the six hourly ECMWF reanalysis data. The disruption at 0 UTC due to the switch to higher-frequency data in the sensitivity experiments is very short lived and does not result in model trends.

## 4.2. Sensitivity Experiments

[45] Two basic considerations are relevant to the organization of the sensitivity experiments: (1) understanding the ocean responses at meso- and submesoscales cannot be achieved in isolation from the understanding of larger-scale responses and (2) because synthetic fields are idealized, comparisons between simulations with more realistic forc-

**Table 1.** Parameters Used in the “Large-Scale Wind” Experiment LsW (Equation (7))<sup>a</sup>

Parameter	Unit	LsW	(NoT)LsW
$A_B$	$\text{ms}^{-1}$	5.5	5.5
$k_B$	$10^{-6} \text{ rad m}^{-1}$	-6	-6
$l_B$	$10^{-6} \text{ rad m}^{-1}$	7	7
$\frac{\lambda_B}{2} = \frac{\pi}{\sqrt{k_B^2 + l_B^2}}$	km	341	341
$\phi_B$	rad	0	0
$c_B$	$\text{ms}^{-1}$	9.5	9.5
Tidal forcing		yes	no

<sup>a</sup>NoT stands for the experiment without tidal forcing.

ing (ECMWF reanalysis data) and idealized forcing are needed. Therefore, two groups of experiments were performed: (1) with different large-scale wind forcing and (2) with different small-scale features in the wind field. The first group also includes the experiments made to demonstrate the difference between realistic and synthetic winds.

[46] The large-scale idealistic forcing aims to present in a simple way the basic large-scale features of the wind field as seen in the SAR-derived wind data (Figure 2). The synthetically generated background wind field pattern  $F_B$  is assumed stationary and given by

$$F_B(x, y) = A_B \cos(k_B x + l_B y + \phi_B) + c_B, \quad (7)$$

where  $x$  and  $y$  are the zonal and meridional coordinates. Parameters in the above equation (Table 1) are specified such that the wind speed gradually increases from  $4 \text{ ms}^{-1}$  in the southeastern corner to  $15 \text{ ms}^{-1}$  in the northwestern corner (Figure 9a). In order to keep the rest of atmospheric forcing as simple as possible, but at the same time close to the actual meteorological situation, we use constant surface temperature, dew point, surface pressure, and cloud cover (see Table 2 for the used values). In the following, the experiment using only the background wind  $F_B$  will be referred to as “large-scale wind” (LsW) experiment.

[47] To demonstrate the coupling between the large-scale wind forcing and tides and the geophysical relevance of the LsW experiment, three additional simulations called “No-wind” (NoW), “Real-wind” (ReW), and “No-tide” (NoT) experiments have been carried out. In the NoW experiment wind speed is set to zero, in the ReW run it is taken from the six hourly ECMWF reanalysis, along with the ECMWF fields of surface temperature and dew point, in the NoT experiment tides were switched off.

## 4.3. Large-Scale Experiments

[48] The dominant southerly wind creates a difference between the sea elevation averaged over one tidal cycle in the LsW and NoW experiments ranging from  $-6$  to  $+20$  cm (no figure is shown here). Largest (positive) differences are simulated around the North Frisian Islands (NFI). Along the East Frisian Islands (EFI) region, the deviations are negative (up to  $-6$  cm), the southerly wind pushing the water out of the Ems Estuary and Jade Bay. The differences between LsW and NoW in the southern zone are relatively small, which is explained by the weaker winds there.

[49] The elevation differences averaged over one tidal cycle between ReW and NoW display a similar trend to

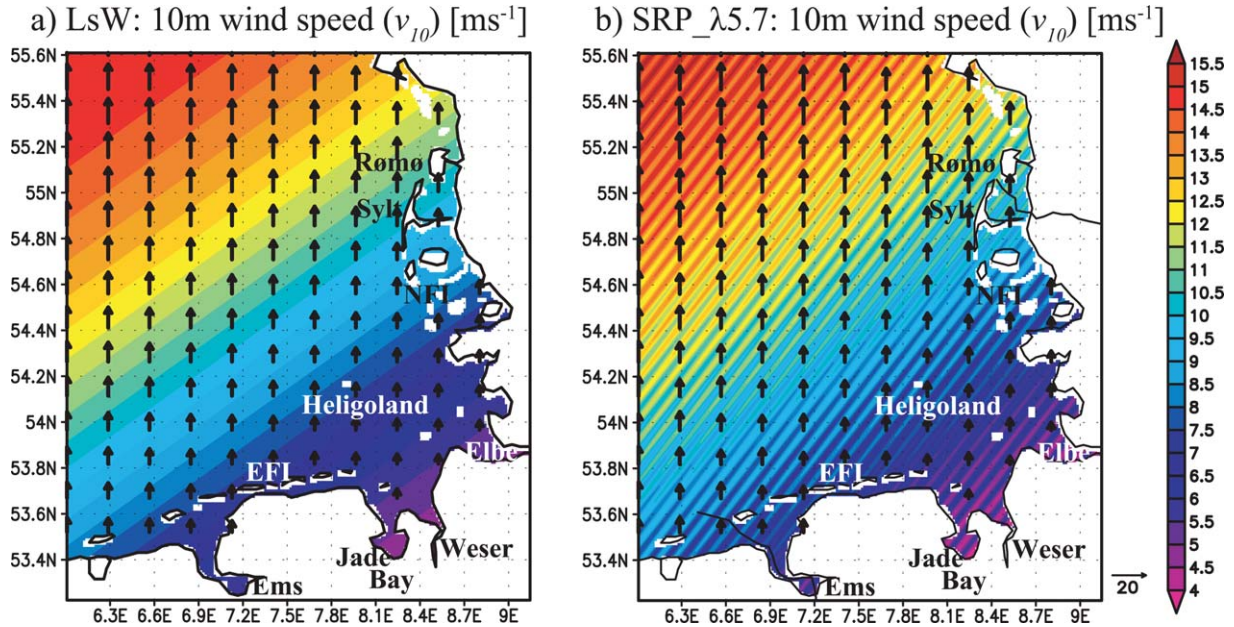


**Figure 9.** (a) Ten meter wind field pattern  $F_B$  used in the experiment with large-scale wind forcing (LsW) for 6 March 2007. The following abbreviations are used: the East Frisian Islands (EFI) and the North Frisian Islands (NFI). (b) Wind field at 10 UTC used in the experiment with small-scale roll pattern of 5.7 km wavelength (SRP\_λ5.7) for 6 March 2007.

that seen in the LsW versus NoW comparison. However, amplitudes are larger ( $-14$  cm) along the EFI and up to  $+25$  cm along the NFI zone, which demonstrates that the temporal variability of the real wind associated with the movement of the low pressure system causes a stronger impact on the German Bight's surface elevation than the stationary forcing. Table 3 gives further quantifications of the simulated differences at four locations (Figure 10) at the times of high (HW) and low water (LW). At the locations A, B, and D the deviations are always positive which means that the water level is higher due to wind forcing. The elevation differences compared to the NoW experiment are higher in the ReW than in the LsW experiment.

[50] The differences in the simulated temperature patterns between the experiments that include a wind component (LsW and ReW) and the wind-free NoW case also agree well. In the offshore area, the wind primarily leads to a water cooling at the surface of up to  $0.4$  K (Figure 10b). Maximum cooling can be found in front of the NFI. Behind these islands, coastal water shows a warming trend of up to  $0.6$  K.

**Table 2.** Atmospheric Forcing Data Used in the Circulation Model

Parameter	Description	Value
t2	2 m temperature	282 K
d2	2 m dewpoint temperature	279.5 K
slp	mean sea level pressure	1000 hPa
tcc	total cloud cover	1
$u_{10}$	zonal velocity component at 10 m	$0 \text{ ms}^{-1}$ (LsW, SRP exps., not ReW)
$v_{10}$	meridional velocity component at 10 m	in $\text{ms}^{-1}$ (depends on the exp.)

[51] The large-scale pattern of SST (Figure 10a) reveals a geometric similarity with the cotidal lines in this area, demonstrating the governing role of Kelvin wave propagation. However, a number of front-like structures are superimposed, demonstrating the role of the mesoscale dynamics. The basic mesoscale features caused by the differences in the wind forcing in the two experiments are the strip-like patterns (about  $10$ – $15$  km wide) with north-south orientation, as well as numerous small-scale features in the coastal zone. Their scales are much smaller than the scales of the input wind and those of the Kelvin wave, which gives an indication of pattern formation due to interaction between winds and tide. To understand this SST distribution, it is instructive to first have a closer look at the NoW experiment (Figures 10a and 10c).

[52] The comparison between the LsW and NoW experiments demonstrates that the vertical velocity  $w$  is most sensitive to variations in the forcing (Figure 10c). The

**Table 3.** Simulated Elevation (See Figure 10 for the Sample Locations)<sup>a</sup>

Location	Stage	Time (UTC)	Elevation (m)		
			NoW	LsW	ReW
(A) Sylt	HW	13.36	0.34	0.42	0.57
	LW	19.57	$-1.38$	$-1.32$	$-1.26$
(B) Heligoland	HW	12.27	0.4	0.43	0.48
	LW	19.06	$-1.52$	$-1.51$	$-1.48$
(C) Norderney	HW	11.45	0.52	0.53	0.53
	LW	18.30	$-1.54$	$-1.56$	$-1.55$
(D) Offshore	HW	12.09	0.06	0.1	0.14
	LW	18.39	$-1.04$	$-1.01$	$-0.98$

<sup>a</sup>HW and LW stands for high and low water.

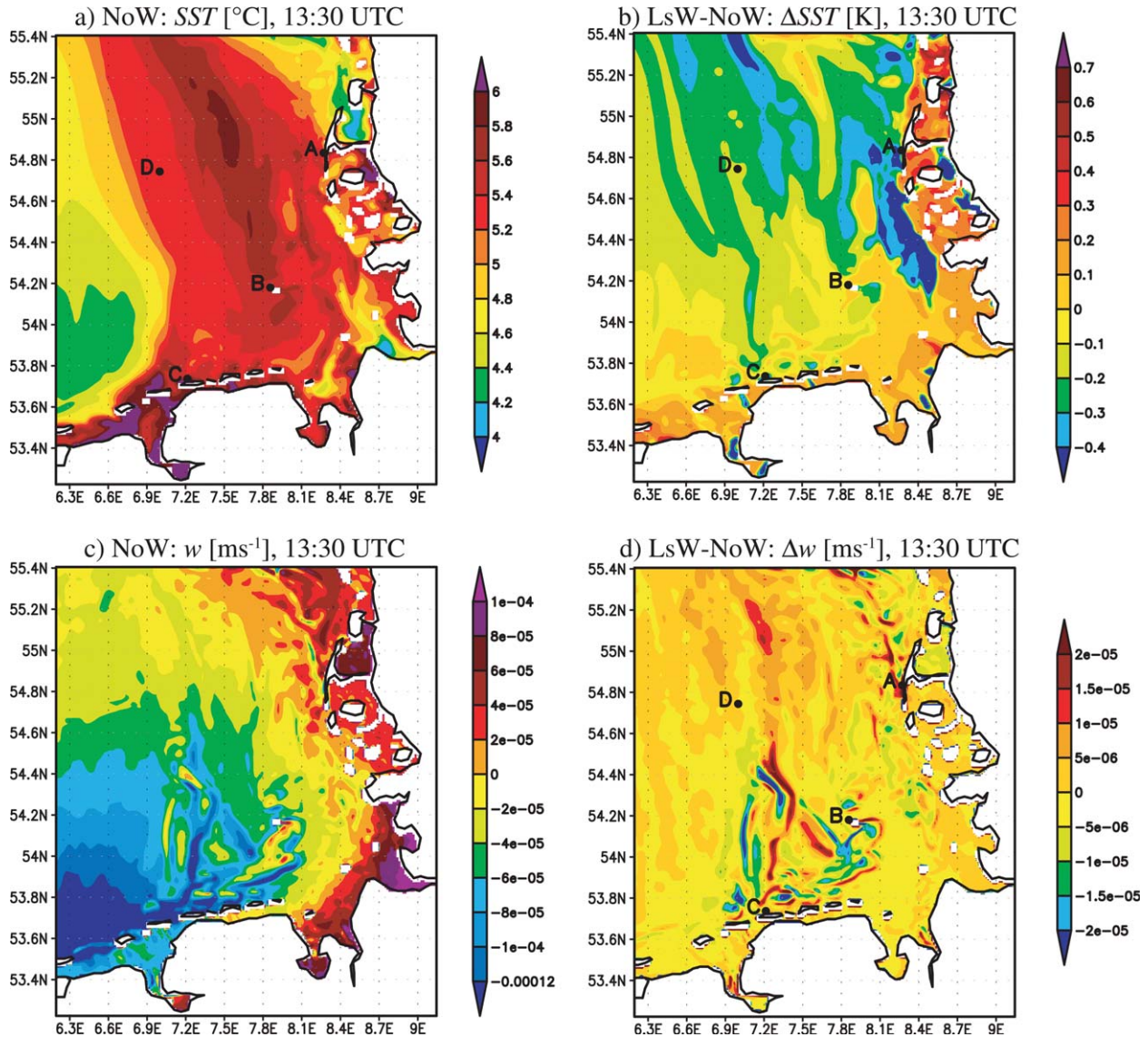


**Figure 10.** (a) Sea surface temperature of the “No-wind” experiment (NoW). (b) The SST-difference pattern between the experiments LsW and NoW. (c) Vertical velocity  $w$  at sea surface of the NoW experiment and (d) the  $w$  difference at the surface layer simulated in LsW and NoW at 13:30 UTC on 6 March 2007. Locations A (Sylt), B (Heligoland), C (Norderney), and D (Offshore) are used in Table 3.

differences in the two experiments (Figure 10d) are primarily due to differences in divergence-convergence of the flow. This affects the vertical mixing and hence the vertical stratification in the water column. It is important to note that the north-south alignment of the vertical velocity is a rather robust feature, which has been simulated under different wind conditions.

[53] The difference between surface currents in the LsW and NoW experiments are very similar to the difference between ReW and NoW experiments (not shown here). The deviations between the two sets of experiments range between  $-0.35$  and  $+0.3$   $\text{ms}^{-1}$  for the LsW experiment and  $-0.4$  and  $+0.35$   $\text{ms}^{-1}$  for the ReW experiment. One can therefore assume that the discussion below using LsW forcing reflects the basic responses characteristics of the real case.

[54] Both wind experiments (LsW and ReW) also show similar patterns of the corresponding statistics (bias and standard deviation) related to the NoW experiment. The largest SST deviations averaged over one tidal period of about 0.5 K are simulated in front of the NFI and are due to the overall cooling. In contrast to the offshore areas, the near-coastal areas (between the barrier islands and the mainland) get warmer in the experiments with nonzero wind (up to  $+0.6$  K), except for some small areas within the Ems and Weser estuaries (up to  $-0.3$  K).

#### 4.4. Ocean Response to Small-Scale Forcing

##### 4.4.1. Synthetic Atmospheric Boundary Layer Roll Forcing

[55] Having shown that the mesoscale patterns account for a substantial component of the circulation in the

**Table 4.** Parameters Used in the Experiments With Small-Scale Roll Pattern (SRP) (Equation (9))<sup>a</sup>

Parameter	Unit	Value in Experiment Number				
		SRP_λ5.7	SRP_λ20	SRP_A <sub>S</sub> 2.5	SRP_Ndir	(NoT) SRP_A <sub>S</sub> 2.5
A <sub>S</sub>	ms <sup>-1</sup>	1	1	2.5	1	2.5
Roll inclination β	°	55	55	55	55	55
k <sub>S</sub>	10 <sup>-4</sup> rad m <sup>-1</sup>	-9.03	-2.57	-9.03	-9.03	-9.03
l <sub>S</sub>	10 <sup>-4</sup> rad m <sup>-1</sup>	6.32	1.8	6.32	6.32	6.32
λ <sub>S</sub> = $\frac{2\pi}{\sqrt{k_S^2+l_S^2}}$	m	5,700	20,000	5,700	5,700	5,700
T <sub>1</sub>	minutes	24.5	75	24.5	24.5	24.5
ω <sub>1</sub> = 2π/T <sub>1</sub>	10 <sup>-3</sup> s <sup>-1</sup>	4.27	1.4	4.27	-4.27	4.27
T <sub>2</sub>	hours	5	5	5	5	5
ω <sub>2</sub> = 2π/T <sub>2</sub>	10 <sup>-4</sup> s <sup>-1</sup>	3.49	3.49	3.49	3.49	3.49
Wind direction	°	180	180	180	360	180
Tidal forcing		yes	yes	yes	yes	no

<sup>a</sup>NoT stands for the experiment without tidal forcing.

German Bight, we address below the following question: Is the mesoscale ocean field substantially affected by the mesoscale transient BLR? In order to answer this question, a synthetically generated wind field  $F$  is constructed below, which is the sum of the background wind field  $F_B$  (equation (7)) and a field of a small-scale sine wave  $F_S$ :

$$F(x, y, t) = F_B(x, y) + F_S(x, y, t) \quad (8)$$

with

$$F_S(x, y, t) = A_S \sin(k_S x + l_S y + \omega_1 t) \cdot \chi(t). \quad (9)$$

[56] This sine wave reproduces the BLR of the SAR case study of 6 March 2007 (see Figures 2a and 9b) and is called the small-scale roll pattern (SRP) in the following.

[57] The function  $\chi(t)$  is a time window that is defined as

$$\chi(t) = \begin{cases} \cos^2\left(\frac{\omega_2}{2}t\right), & t_1 \leq t \leq t_2 \\ 0, & \text{otherwise.} \end{cases} \quad (10)$$

[58] The parameters of the SRP are listed in Table 4. The frequency  $\omega_2$  describes the appearance and disappearance of the SRP, that is, it gives a temporal window in which the variations occur. Period  $T_2 = 2\pi/\omega_2$  was chosen such that the atmospheric perturbation appears during a time window of 5 h between  $t_1$  and  $t_2$  centered at the time of acquisition of the SAR-image, that is, 7.30 and 12.30 UTC with maximum amplification at 10 UTC.

[59] The wave numbers  $k_S$  and  $l_S$  of experiments SRP\_λ5.7, SRP\_A<sub>S</sub>2.5 and SRP\_Ndir (see Table 4) were chosen such that the wavelength  $\lambda_S$  is 5700 m, which is the mean value calculated from the two-dimensional FFT (see Figure 5). Accordingly, the inclination of the sine wave is 55°. The wavelength  $\lambda_S$  in experiment SRP\_λ20 was defined as 20 km, which is the maximum wavelength for such phenomena reported in *Etling and Brown* [1993].

[60] The period  $T_1 = 2\pi/\omega_1$  can be calculated by equations (5) and (6), assuming that the pattern was advected by the low-level jet at 1000 m. According to the data presented in the SAR case study, the period is in the range of 17–26 min. Thus, a period  $T_1$  of 24.5 min was chosen for the experiments with  $\lambda_S = 5700$  m. Correspondingly, 75 min

was assigned for  $T_1$  in the experiment with the 20 km wave.

[61] The 10 m wind direction is southerly at each grid point except of experiment SRP\_Ndir, where the direction was changed to northerly. The modification of the wind direction at 10 m height also implies a 180° rotation of the vector  $\mathbf{V}_{adv}$  (Figure 7) to take into account the Ekman veering, i.e., the clockwise wind rotation from the ground to the upper levels of the atmosphere. To adjust the propagation direction of the wind perturbations accordingly, the sign of frequency  $\omega_1$  was changed in the SRP\_Ndir experiment.

[62] Figure 9b shows the synthetically generated wind field of experiment SRP\_λ5.7 at 10 UTC within the model domain. Background wind speed as well as wind direction are constant in time, thus only the small-scale sine wave of the wind magnitude is transient.

#### 4.4.2. Horizontal Patterns of the Oceanic Response

[63] The simulations with SRP were performed for one day starting on 6 March 2007 at 0 UTC. The model output was produced with 3 min time discretization. In the following, the SRP and LsW experimental results are compared in order to estimate the consequences of individual changes in the forcing. The maximum deviations from the LsW experiment were observed between 10.30 and 11 UTC, and are well recognized in Figure 11 by the regularly distributed streaks with the same wavelength and inclination as in the wind forcing. In general, the response to the mesoscale wind forcing seen in the surface current (*sfc* in the figures) and sea surface temperature is stronger in the coastal areas and weaker in the interior of the German Bight. Furthermore, response effects are not symmetric with respect to the wind direction, as demonstrated in the comparison between experiments with southerly wind (Figures 11a and 11b) and northerly wind (Figures 11g and 11h).

[64] The deviations of the surface current magnitude (left column of Figure 11) caused by the mesoscale wind variability are relatively small (of the order of 0.01 ms<sup>-1</sup>) because of the small wind fluctuations ( $\pm 2.5$  ms<sup>-1</sup> maximum in the experiment with increased SRP amplitude  $A_S$ , see Figure 11e). The strongest response is observed in the coastal zone around Sylt, as well as in the northwestern corner of the model area.

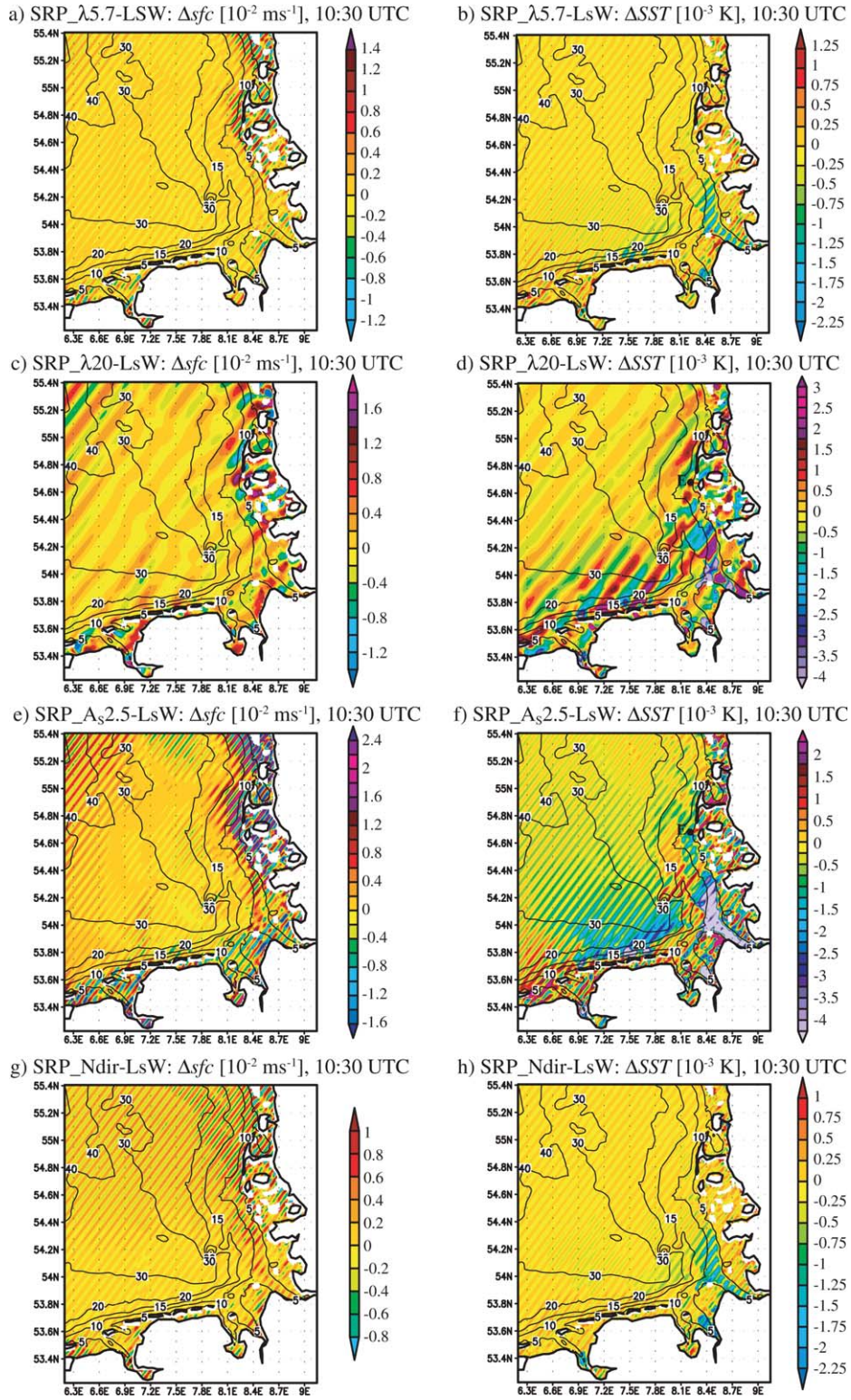


**Figure 11.** Difference patterns of the surface current magnitude ( $\Delta sfc$ , left column) and the sea surface temperature ( $\Delta SST$ , right column) between the different SRP experiments and LsW at 10:30 UTC on 6 March 2007. The parameters of the SRP experiments listed in Table 4 are described in the text. The black contour lines mark the German Bight bathymetry in meters.

[65] The experiment with an SRP of 20 km wavelength shows a stronger response (Figure 11c). The simulations with larger BLR period of 75 min enabled more time for

the upper mixed layer to react, resulting in SST perturbation amplitudes of up to 3 times larger. In experiments with stationary BLR (not shown here) the response is even

stronger. Although the surface current deviations are nearly in the same range as in experiment SRP\_λ5.7, the SST deviations increased by a factor of 4. In sensitivity experiments with northerly wind (Figure 11g), the surface current in the northern part of the model domain, as well as in the EFI area are more affected by the mesoscale oscillations.

[66] The impact of mesoscale wind forcing on the sea surface temperature (right column of Figure 11) is better pronounced in the coastal area within the 30 m isobath. The strongest response as well as nontrivial response patterns are observed in the area of the Elbe estuary and the EFI area. Maximum deviations are very small (of the order of 0.001 K); however, they are useful as indicators of areas of relatively stronger sensitivity to small-scale changes in the wind forcing. The overall result is that the major response of the model reveals a water cooling in the estuaries (most pronounced in the Elbe Estuary), as well as to the north of the EFI (Figure 11b). The change of the wind direction (compare Figures 11h to 11b) does not affect the SST response substantially. An increased roll wavelength or an increased roll amplitude intensifies the deviations along the coasts.

[67] The rms difference between surface currents in the SRP\_λ5.7 and SRP\_A<sub>S</sub>2.5 experiments shows a maximum of 1 cm s<sup>-1</sup>, which is located in the Wadden Sea. The interior of the German Bight is almost unaffected. Obviously, the response of the surface current is only transient, without pronounced influence on the mean for one tidal period circulation.

#### 4.4.3. Upper Mixed Layer Responses to Boundary Layer Rolls

[68] Although the simulated differences between the sensitivity experiments are very weak, it is interesting to analyze the behavior of the vertical profiles of temperature and vertical velocity (Figure 12). At location E with coordinates 54.67°N, 8.2°E (see map in Figures 11e and 11f for the position), where the depth is about 7 m, the temporal oscillations in the vertical velocity with the periodicity of the forcing signal tend to enhance mixing in the experiment SRP\_A<sub>S</sub>2.5, thus producing a cooling trend in the upper layer and a warming beneath. In about 2–3 h, the warming reaches the bottom. With the time progressing, the atmospheric perturbation decreases and the vertical stratification tends to the state before the oscillation has been imposed, that is, no pronounced residual effects were caused by the transient changes of surface wind.

[69] To examine whether this can be viewed as a “standard” response, we next present similar simulations resulting from the SRP\_λ20 experiment in which the wave length was chosen as  $\lambda = 20$  km and the amplitude as  $A_S = 2.5$  ms<sup>-1</sup> (compare Figures 12a and 12c with Figures 12b and 12d, respectively). The difference to the case of SRP\_A<sub>S</sub>2.5 ( $\lambda = 5.7$  km,  $A_S = 2.5$  ms<sup>-1</sup>) demonstrates lower frequency in the ocean response. This is seen as a recurrent appearance of stronger and weaker changes in temperature stratification. This variability propagates downward. As in the case of the SRP\_λ20 experiment the stratification trend reverses at about 4–5 m. However, in contrast to the former case, no unidirectional (cooling) trend is observed in the surface layer at about 11–14 UTC, while the temperature change is not pronounced in the bot-

tom layer, either at about 13–14 UTC. Furthermore, the lower frequency in the forcing resulted in a response that was almost 3 times larger than in the SRP\_A<sub>S</sub>2.5 experiment.

#### 4.4.4. The Effect of Tides

[70] There is a need to explain the reasons for the relatively small oceanic response to the BLR simulated in the model. Such small responses would not be detected in field observations and hence may not be relevant for the ocean boundary layer. However, in the case of large perturbations induced by strong BLR events, the changes in circulation or stratification could also create a signature in the SAR images or in other data. In this context, one should remember that the observed modulations in SAR images can be either caused by variations of the near-surface wind or ocean features (strong gradients of currents, internal waves, or upwelling). The fact that we use a prescribed atmospheric forcing (no coupling between atmosphere and ocean is simulated in this study) excludes the possibility of fully addressing the coupling between atmospheric and oceanic boundary layers. Furthermore, no coupled wave-circulation model has been used here, thus the chain of processes that govern the penetration of atmospheric signals into the ocean is only partially simulated.

[71] We can, however, use our model to perform numerical simulations to identify the conditions under which BLR can have stronger impact in the ocean boundary layer. The hypothesis is that in areas with complex bottom topography and strong tidal currents the influence of BLR is masked; therefore, we analyze below the results from the NoT experiment. In order to make clear the contribution of tides and to “remove” the effect of large-scale wind forcing, we show in Figure 13 the difference between experiment SRP\_A<sub>S</sub>2.5 and LsW when forced without tides (Figures 13a and 13c) and with tides (Figures 13b and 13d).

[72] The following conclusions are obvious from these results: (1) tides reduce the spatial gradients (larger contrasts are seen in Figure 13a compared to the ones in Figure 13b), which is a demonstration of the role of tidal mixing, (2) tides explain the enhancement of responses west of the NFI; without tides, surface currents in Figure 13a do not show pronounced spatial patterns, and (3) the temperature response in estuaries is stronger in the absence of tides, which proves that tidal mixing in these areas reduces the ability of the model to create the estuarine patterns seen in Figure 13c. The latter result would suggest that nontidal seas are better candidates for the study of ocean responses to BLR.

#### 4.4.5. Synthesis

[73] The above results are summarized below in two major points.

[74] 1. The mixing in the German Bight is primarily dominated by tides. Therefore, the small oscillations of wind cannot substantially affect the vertical stratification. In strongly stratified ocean this response could be stronger.

[75] 2. The numerical simulations enable to detect propagating striplike patterns in the ocean with the scales of BLR. However, these small-scale anomalies tend to nullify each other. This additionally reduces the responses because trends cancel at very short distances.

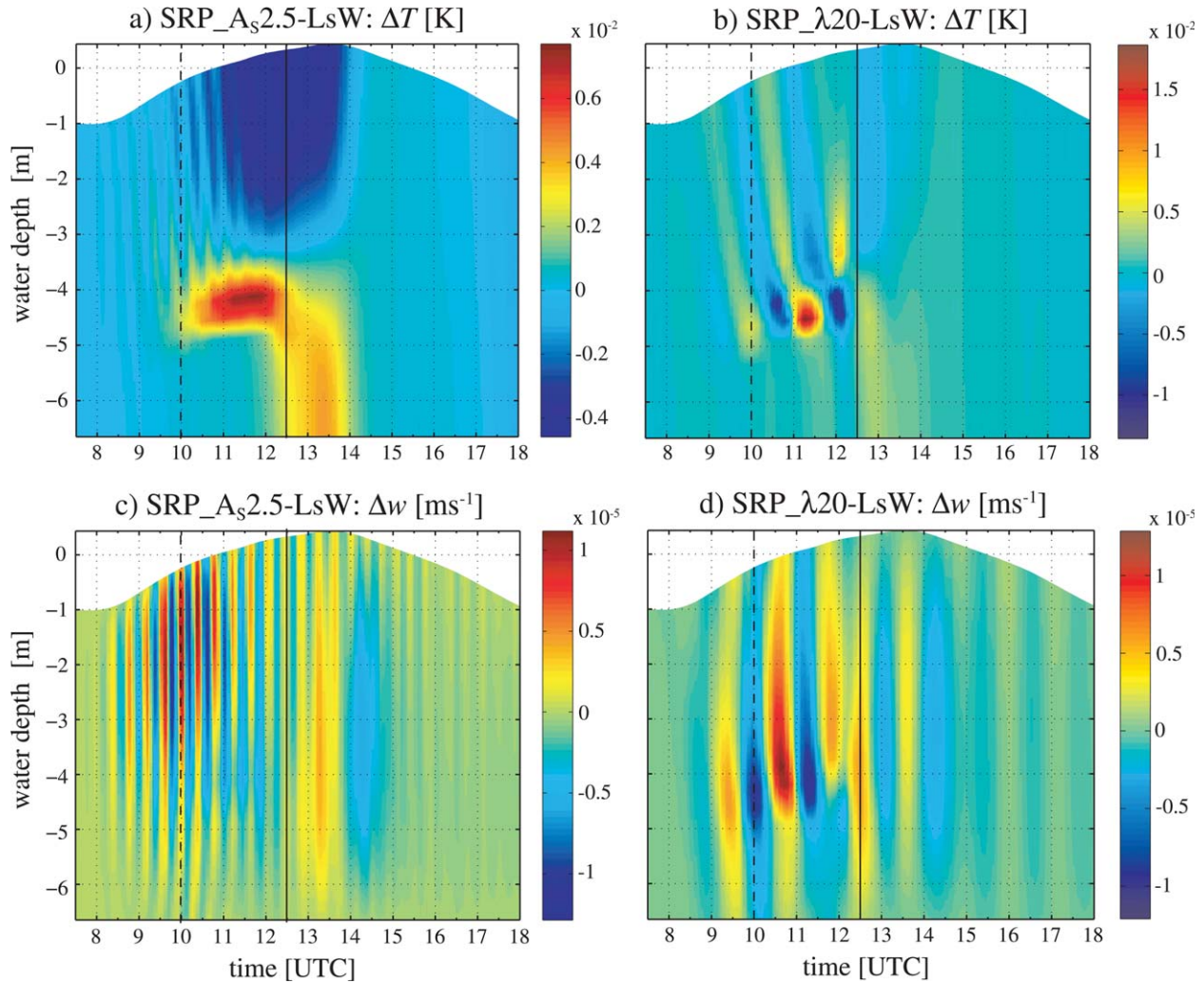


**Figure 12.** Time versus depth variability in location E (see Figures 11d and 11f). Differences between the experiment with small-scale roll patterns with amplitude of  $2.5 \text{ ms}^{-1}$  (SRP\_A52.5) and the experiment LsW are presented for (a) temperature and (c) vertical velocity on 6 March 2007. The atmospheric wind perturbation appears between 7.30 and 12.30 (black solid line) with maximum amplification at 10 UTC (black dashed line). (b and d) Same as Figures 12a and 12c, but for the difference between experiment SRP\_lambda20 with amplitude of  $1 \text{ ms}^{-1}$  and wavelength of 20 km, and the experiment LsW.

[76] The above conclusions do not mean that all possible mesoscale disturbances in the atmospheric forcing are unimportant. Our numerical simulations were tailored to maximally correspond to the characteristic of atmospheric BLR during one particular day. It can be expected that larger magnitudes in the oscillations of wind would create stronger responses. In addition, the applied perturbations were active only over a short period. The FINO 1 data show, however, that high-frequency variations in the wind forcing may dominate over longer times. The present study suggests that the addressed spectral components, which are not contained in most of the operational forecast systems, could be a factor in the mixing processes in shallow coastal areas. Furthermore, coupled ocean-atmospheric physics should account in more detail for the changes in the atmospheric boundary layer and include consideration of sea surface roughness. Therefore, the considerations above should be understood as an initial

answer to the problem formulated earlier as to whether the short-lived mesoscale atmospheric disturbances associated with BLR can substantially affect the mesoscale ocean field.

## 5. Summary and Conclusions

[77] Small-scale wind variations were investigated in a case study based on a SAR image acquired on 6 March 2007 at 9.55 UTC. An effort has been made to link spatial variations from the SAR-derived wind field to temporal (short-period) variations observed at the research platform FINO 1 during the same day. The SAR-derived wind variations were likely indicative of atmospheric BLR having a wavelength of 5–6 km that were caused by the inflection point instability, which is associated with the inflection point in the cross-roll component of the mean large-scale wind profile. A sliding discrete Fourier transform analysis

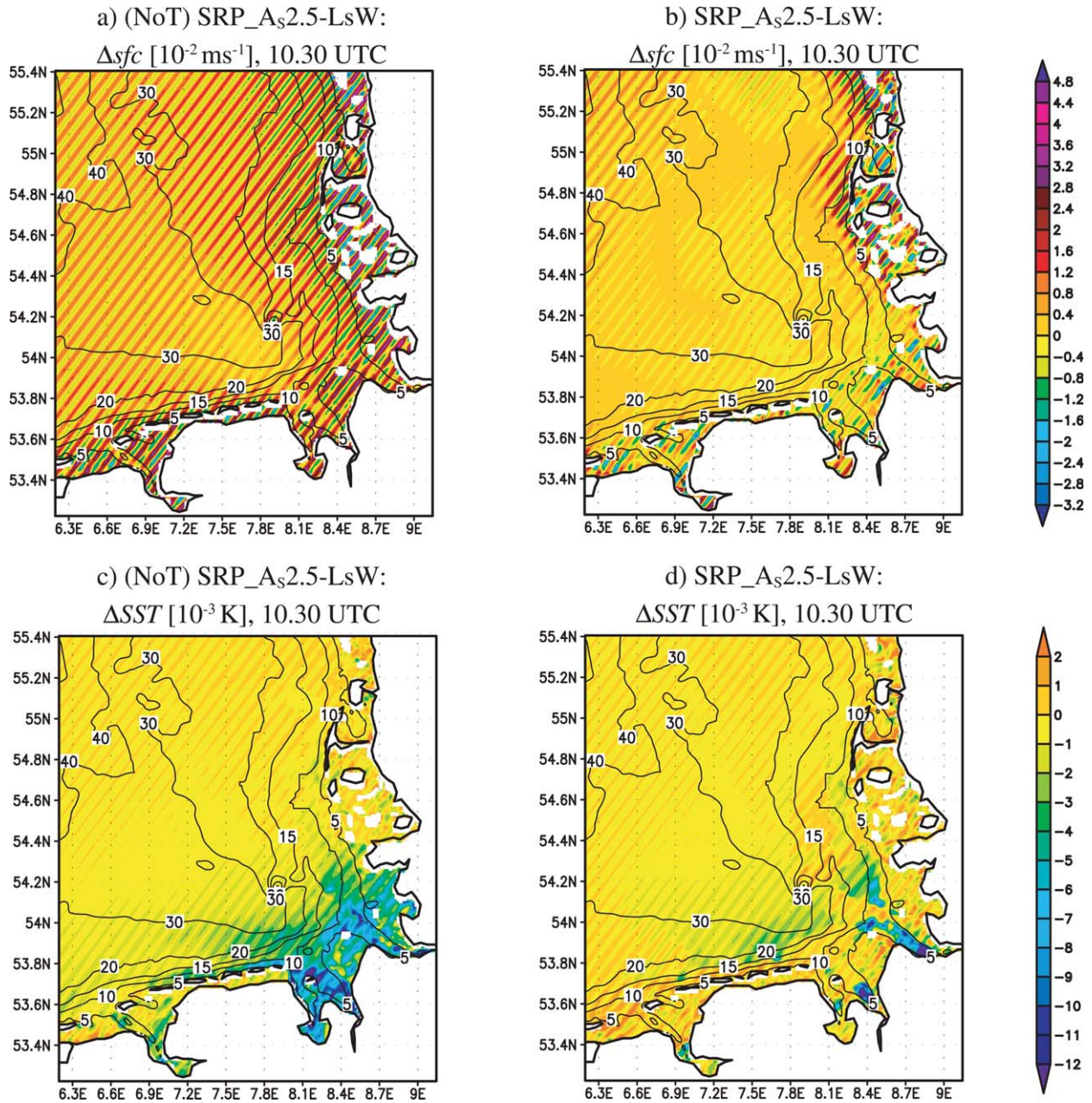


**Figure 13.** (a and b) Difference patterns of the sfc magnitude between the experiment with small-scale roll pattern (SRP) and without (LsW) for 10.30 UTC. (a) Without tidal forcing. (b) With tidal forcing. (c and d) Same as Figures 13a and 13b but for SST.

of FINO 1 data at 33 m reveals wind variation periods of 17–26 min between 9 and 13 UTC. This was in a good agreement with the estimated period resulting from the propagation of BLR caused by a low-level jet coming from the southwest with a speed of 23–28  $\text{ms}^{-1}$ .

[78] In a series of numerical experiments, the observed wind variations called SRP were synthetically generated to investigate the impact of mesoscale atmospheric perturbations on the hydrodynamic processes in the German Bight. In a first step, the effects of large-scale wind forcing were investigated, which showed that the synthetically generated background wind field  $F_B$  was able to generate the same

characteristic ocean response patterns as the more realistic ECMWF field. Furthermore, it appeared that the large-scale wind was responsible for substantial mesoscale changes in the vertical velocity and large responses in the ocean fields. The patterns and scales of mesoscale features did not have a counterpart in the wind forcing, demonstrating a new pattern-formation process.

[79] The experiments with SRP showed that the impact of small streaklike wind variations was weak on the surface current and negligible on the sea surface temperature. The anomalies are concentrated in the shallow water regions along the coasts. The strongest impact can be observed

near Sylt in experiment SRP\_<math>A\_S</math> 2.5. Here, the maximum deviations of current velocity are 0.02–0.05 ms<sup>-1</sup> at 10.30 UTC, which are about 10–15% of the reference (LsW) current. However, the maximum temperature deviations located around Sylt and in the Elbe estuary are only 0.005–0.01 K from 10.30 to 11.30 UTC. This shows that changes of the surface current magnitude are detectable, but only for a short time. Direct measurement of these BLR-induced changes therefore represents a major oceanographic challenge. However, stronger impacts on the upper ocean parameters can be expected if the BLR have larger wavelength, lower frequency (enabling enough time for the perturbations to develop a response in the upper ocean), higher amplitudes (<math>A\_S</math>), and also occur in nontidal basins.

[80] The simulated upper-ocean responses in this paper seem too weak to be able to explain substantial modulations in radar imagery caused by BLR-induced dynamics. There is then a reasonable question: Could it be that the modeling presented here is underestimating the ocean response to atmospheric BLR. There are some reasons to give a positive answer to this question. We admit that the model used here cannot address all basic processes, which potentially govern the coupling between atmospheric boundary layer rolls and small-scale processes in the ocean surface layer. One good solution would be to either use a coupled atmosphere waves circulation model, or use at least as an intermediate step a coupled wave-circulation model forced in the same fashion as in the present work. Better resolution has also to be used in order to sufficiently address small-scale roughness on the ocean surface. Our preliminary work shows that the effects of the coupling between wind, waves, and circulation are not negligible in the coastal zone, and this is one potential area for future development, in particular, in nontidal basins where signals will be not masked by mixing due to tides.

[81] The circulation modeling used in the present work gives indications of the following: (1) specific pattern formation associated with the BLR and (2) increased mixing in the upper layer, which is a first step toward improved understanding of the coupling between atmospheric BLR and small-scale processes at the ocean surface. As a result, the next challenge is to investigate whether these BLR-induced oceanic responses can be observed directly. Several techniques described in the recent literature (Romeiser et al. [2010]; Matthews and Yoshikawa [2012] (which is a recent paper using very high-resolution HF radar)) hold promise in this regard. However, any attempt to resolve this important issue will require careful event selection, most likely from within a region of little or no tidal flow.

[82] **Acknowledgments.** Thanks to the Federal Maritime and Hydrographic Agency (BSH) for providing data from the research platform FINO 1 and the MARNET station “Ems.” The radiosonde data were supplied by the University of Wyoming. Forcing data have been provided by the European Centre for Medium-Range Weather Forecasts. Thanks are due to J. Matthews and two anonymous reviewers for their valuable comments and suggestions on how to improve the paper.

## References

Alpers, W., and B. Brümmer (1994), Atmospheric boundary layer rolls observed by the synthetic aperture radar aboard the ERS-1 satellite, *J. Geophys. Res.*, 99(C6), 12,613–12,621, doi:10.1029/94JC00421.

- Alpers, W., and I. Hennings (1984), A theory of the imaging mechanism of underwater bottom topography by real and synthetic aperture radar, *J. Geophys. Res.*, 89(C6), 10,529–10,546, doi:10.1029/JC089iC06p10529.
- Beaucage, P., A. Glazer, J. Choinsard, W. Yu, M. Bernier, R. Benoit, and G. Lafrance (2007), Wind assessment in a coastal environment using synthetic aperture radar satellite imagery and a numerical weather prediction model, *Can. J. Remote Sens.*, 33(5), 368–377, doi:10.5589/m07-043.
- Burchard, H., and K. Bolding (2002), GETM, A General Estuarine Transport Model: Scientific Documentation, Inst. for Environ. and Sustainability, Joint Res. Centre, Ispra, Italy.
- Chelton, D., M. Schlax, M. Freilich, and R. Milliff (2004), Satellite measurements reveal persistent small-scale features in ocean winds, *Science*, 303(5660), 978–983, doi:10.1126/science.1091901.
- Egbert, G., and S. Erofeeva (2002), Efficient inverse modeling of barotropic ocean tides, *J. Atmos. Oceanic Technol.*, 19(2), 183–204, doi:10.1175/1520-0426(2002)019<0183:EIMOBO>2.0.CO;2.
- Etling, D., and R. Brown (1993), Roll vortices in the planetary boundary layer: A review, *Boundary Layer Meteorol.*, 65(3), 215–248, doi:10.1007/BF00705527.
- Foster, R. (2005), Why rolls are prevalent in the hurricane boundary layer, *J. Atmos. Sci.*, 62(8), 2647–2661, doi:10.1175/JAS3475.1.
- Fu, L., and B. Holt (1982), Seasat Views Oceans and Sea Ice With Synthetic-Aperture Radar, JPL publication, Calif. Inst. of Technol., Jet Propulsion Laboratory.
- Ginis, I., A. Khain, and E. Morozovsky (2004), Effects of large eddies on the structure of the marine boundary layer under strong wind conditions, *J. Atmos. Sci.*, 61(24), 3049–3064, doi:10.1175/JAS-3342.1.
- Gryschka, M., and S. Raasch (2005), Roll convection during a cold air outbreak: A large eddy simulation with stationary model domain, *Geophys. Res. Lett.*, 32, L14805, doi:10.1029/2005GL022872.
- Gryschka, M., C. Drüe, D. Etling, and S. Raasch (2008), On the influence of sea-ice inhomogeneities onto roll convection in cold-air outbreaks, *Geophys. Res. Lett.*, 35, L23804, doi:10.1029/2008GL035845.
- Horstmann, J., and W. Koch (2005), Comparison of SAR wind field retrieval algorithms to a numerical model utilizing ENVISAT ASAR data, *IEEE J. Oceanic Eng.*, 30(3), 508–515.
- Horstmann, J., W. Koch, S. Lehner, and R. Tonboe (2002), Ocean winds from RADARSAT-1 scansar, *Can. J. Remote Sens.*, 28(3), 524–533, doi:10.5589/m02-043.
- Horstmann, J., H. Schiller, J. Schulz-Stellenfleth, and S. Lehner (2003), Global wind speed retrieval from SAR, *IEEE Trans. Geosci. Remote Sens.*, 41(10), 2277–2286, doi:10.1109/TGRS.2003.814658.
- Jacobsen, E., and R. Lyons (2003), The sliding DFT, *IEEE Signal Process. Mag.*, 20(2), 74–80, doi:10.1109/MSP.2003.1184347.
- Katsaros, K., P. Vachon, P. Black, P. Dodge, and E. Uhlhorn (2000), Wind fields from SAR: Could they improve our understanding of storm dynamics?, *Johns Hopkins APL Tech. Dig.*, 21(1), 86–93.
- Koch, W. (2004), Directional analysis of SAR images aiming at wind direction, *IEEE Trans. Geosci. Remote Sens.*, 42(4), 702–710, doi:10.1109/TGRS.2003.818811.
- Koch, W., and F. Feser (2006), Relationship between SAR-derived wind vectors and wind at 10-m height represented by a mesoscale model, *Mon. Weather Rev.*, 134(5), 1505–1517, doi:10.1175/MWR3134.1.
- Kozlov, I. E., V. N. Kudryavtsev, J. A. Johannessen, B. Chapron, I. Dailidenè, and A. G. Myasoedov (2012), ASAR imaging for coastal upwelling in the Baltic Sea, *Adv. Space Res.*, 50(8), 1125–1137, doi:10.1016/j.asr.2011.08.017.
- Kropfli, R., L. Ostrovski, T. Stanton, E. Skirta, A. Keane, and V. Irisov (1999), Relationships between strong internal waves in the coastal zone and their radar and radiometric signatures, *J. Geophys. Res.*, 104(C2), 3133–3148, doi:10.1029/98JC02549.
- Langmuir, I. (1938), Surface motion of water induced by wind, *Science*, 87(2250), 119–123.
- Leibovich, S. (1983), The form and dynamics of Langmuir circulations, *Annu. Rev. Fluid Mech.*, 15(1), 391–427, doi:10.1146/annurev.fl.15.010183.002135.
- Matthews, J. P., and Y. Yoshikawa (2012), Synergistic surface current mapping by spaceborne stereo imaging and coastal HF radar, *Geophys. Res. Lett.*, 39, L17606, doi:10.1029/2012GL052546.
- Monaldo, F., D. Thompson, W. Pichel, and P. Clemente-Colón (2004), A systematic comparison of QuikSCAT and SAR ocean surface wind speeds, *IEEE Trans. Geosci. Remote Sens.*, 42(2), 283–291, doi:10.1109/TGRS.2003.817213.

- Morrison, I., S. Businger, F. Marks, P. Dodge, and J. Businger (2005), An observational case for the prevalence of roll vortices in the hurricane boundary layer, *J. Atmos. Sci.*, 62(8), 2662–2673, doi:10.1175/JAS3508.1.
- Müller, G., B. Brümmer, and W. Alpers (1999), Roll convection within an Arctic cold-air outbreak: Interpretation of in situ aircraft measurements and spaceborne SAR imagery by a three-dimensional atmospheric model, *Mon. Weather Rev.*, 127(3), 363–380, doi:10.1175/1520-0493(1999)127<0363:RCWAAC>2.0.CO;2.
- Portabella, M., A. Stoffelen, and J. Johannessen (2002), Toward an optimal inversion method for synthetic aperture radar wind retrieval, *J. Geophys. Res.*, 107(C8), 1–13, doi:10.1029/2001JC000925.
- Romeiser, R., J. Johannessen, B. Chapron, F. Collard, V. Kudryavtsev, H. Runge, and S. Suchandt (2010), Direct surface current field imaging from space by Along-Track InSAR and Conventional SAR, edited by V. Barale, J.F.R. Gower, and L. Alberotanza, *Oceanography From Space*, pp. 73–91, Springer Verlag, Berlin.
- Signell, R., J. Chiggiato, J. Horstmann, J. Doyle, J. Pullen, and F. Askari (2010), High-resolution mapping of Bora winds in the northern Adriatic Sea using synthetic aperture radar, *J. Geophys. Res.*, 115, C04020, doi:10.1029/2009JC005524.
- Staneva, J., E. Stanev, J. Wolff, T. Badewien, R. Reuter, B. Flemming, A. Bartholomä, and K. Bolding (2009), Hydrodynamics and sediment dynamics in the German Bight. A focus on observations and numerical modelling in the East Frisian Wadden Sea, *Cont. Shelf Res.*, 29(1), 302–319, doi:10.1016/j.csr.2008.01.006.
- Stoffelen, A., and D. Anderson (1997), Scatterometer data interpretation: Measurement space and inversion, *J. Atmos. Oceanic Technol.*, 14(6), 1298–1313, doi:10.1175/1520-0426(1997)014<1298:SDIMSA>2.0.CO;2.
- Taylor, G. I. (1938), The spectrum of turbulence, *Proc. R. Soc. A*, 164(919), 476–490, doi:10.1098/rspa.1938.0032.
- Thompson, T., W. Liu, and D. Weissman (1983), Synthetic aperture radar observation of ocean roughness from rolls in an unstable marine boundary layer, *Geophys. Res. Lett.*, 10(12), 1172–1175, doi:10.1029/GL010i012p01172.
- Thorpe, S. (2004), Langmuir circulation, *Ann. Rev. Fluid Mech.*, 36, 55–79, doi:10.1146/annurev.fluid.36.052203.071431.
- Wurman, J., and J. Winslow (1998), Intense sub-kilometer-scale boundary layer rolls observed in Hurricane Fran, *Science*, 280(5363), 555–557, doi:10.1126/science.280.5363.555.
- Young, G., D. Kristovich, M. Hjelmfelt, and R. Foster (2002), Rolls, streets, waves and more: A review of quasi-two-dimensional structures in the atmospheric boundary layer, *Bull. Am. Meteorol. Soc.*, 83, 997–1013, doi:10.1175/1520-0477(2002)083<0997:RSWAMA>2.3.CO;2.
- Zhang, J., K. Katsaros, P. Black, S. Lehner, J. French, and W. Drennan (2008), Effects of roll vortices on turbulent fluxes in the hurricane boundary layer, *Boundary Layer Meteorol.*, 128(2), 173–189, doi:10.1007/s10546-008-9281-2.